

THREE-DIMENSIONAL DYNAMIC SOIL–STRUCTURE INTERACTION ANALYSIS IN THE TIME DOMAIN

XIONG ZHANG¹, J. L. WEGNER^{2,*} AND J. B. HADDOW²

¹*Department of Engineering Mechanics, Tsinghua University, Beijing 100084, People's Republic of China*

²*Department of Mechanical Engineering, University of Victoria, PO Box 3055, Victoria, B.C., Canada V8W 3P6*

SUMMARY

A new numerical procedure is proposed for the analysis of three-dimensional dynamic soil–structure interaction in the time domain. In this study, the soil is modelled as a linear elastic solid, however, the methods developed can be adapted to include the effects of soil non-linearities and hysteretic damping in the soil. A substructure method, in which the unbounded soil is modelled by the scaled boundary finite-element method, is used and the structure is modelled by 8–21 variable-number-node three-dimensional isoparametric or subparametric hexahedral curvilinear elements. Approximations in both time and space, which lead to efficient schemes for calculation of the acceleration unit-impulse response matrix, are proposed for the scaled boundary finite-element method resulting in significant reduction in computational effort with little loss of accuracy. The approximations also lead to a very efficient scheme for evaluation of convolution integrals in the calculation of soil–structure interaction forces. The approximations proposed in this paper are also applicable to the boundary element method. These approximations result in an improvement over current methods. A three-dimensional Dynamic Soil–Structure Interaction Analysis program (DSSIA-3D) is developed, and seismic excitations (S-waves, P-waves, and surface waves) and externally applied transient loadings can be considered in analysis. The computer program developed can be used in the analysis of three-dimensional dynamic soil–structure interaction as well as in the analysis of wave scattering and diffraction by three-dimensional surface irregularities. The scattering and diffraction of seismic waves (P-, S-, and Rayleigh waves) by various three-dimensional surface irregularities are studied in detail, and the numerical results obtained are in good agreement with those given by other authors. Numerical studies show that the new procedure is suitable and very efficient for problems which involve low frequencies of interest for earthquake engineering. Copyright © 1999 John Wiley & Sons Ltd

KEY WORDS: soil–structure interaction; coupling method; wave scattering; earthquake engineering; numerical method

1. INTRODUCTION

The various numerical methods developed for the analysis of dynamic soil–structure interaction during the last quarter century can be classified into two main groups; the direct method and the substructure method. In the direct method, the structure and a finite, bounded soil zone adjacent

* Correspondence to: J. L. Wegner, Department of Mechanical Engineering, University of Victoria, P.O. Box 3055, Victoria, B.C., Canada V8W 3P6.

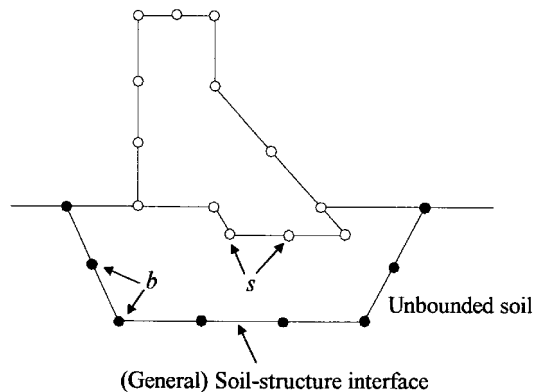


Figure 1. Structure-soil system

to the structure (near field) are modelled by the standard finite-element method and the effect of the surrounding unbounded soil (far field) is analysed approximately by imposing transmitting boundaries along the near-field/far-field interface. Many kinds of transmitting boundaries have been developed over the past two decades to satisfy the radiation condition, such as a viscous boundary,¹ a superposition boundary,² and several others.³

In the substructure method, the soil-structure system is divided into two substructures: a structure which may include a portion of non-linear soil or soil with an irregular boundary, and the unbounded soil.^{4,5} These substructures are connected by the general soil-structure interface (See Figure 1). The unbounded soil is assumed to be linear but the structure could be non-linear. Generally the non-linear soil adjacent to the structure can be treated as a part of the structure, so non-linearity of the soil adjacent to the structure could also be included if necessary.

Usually a dynamic soil-structure interaction analysis by the substructure method can be performed in three steps as follows:

1. Determination of seismic free-field input motion along the general soil-structure interface. The seismic free-field input motion can be determined by free-field site analysis.^{4,6}
2. Determination of the reaction of the unbounded soil on the general soil-structure interface in the form of a displacement-force relationship.
3. Analysis of the bounded soil-structure system under the action of the externally applied transient loading and the ground interaction force determined by steps 1 and 2.

The reaction of the unbounded soil on the general soil-structure interface is represented by a boundary condition in the form of a force-displacement relationship, which is global in both space and time. The boundary-element method is a powerful procedure for modelling the unbounded medium since only the boundaries of the unbounded medium are discretized so that the spatial dimension is reduced by one, and the radiation condition is satisfied automatically as a part of the fundamental solution. Based on the substructure method, many hybrid methods (coupling methods)⁷⁻⁹ have been developed where the structure and an adjacent finite region of the soil are discretized by the standard finite-element method while the unbounded soil is modelled by the boundary-element method. However, it is very difficult to derive the fundamental

solutions for many cases. The scaled boundary finite-element method,¹⁰ which is the alias of the consistent infinitesimal finite-element cell method,¹¹ combines the advantages of the boundary-element method and the finite-element method, and no fundamental solution is required. It is exact in the radial direction, converges to the exact solution in the finite-element sense in the circumferential direction, and is rigorous in both space and time.

In this paper a new three-dimensional dynamic soil-structure interaction procedure is developed where the scaled boundary finite-element method is used to model the unbounded soil while the structure is modelled by 8–21 variable-number-node three-dimensional isoparametric or subparametric hexahedral curvilinear elements.¹² Approximations in both time and space are proposed for the scaled boundary finite-element method to reduce the computational effort required for practical engineering problems. Approximation in time leads to an efficient scheme for evaluation of convolution integrals and approximation in space leads to a sparse unit-impulse response matrix, so that the computational efforts required for the calculation of the unit-impulse response matrix and the ground interaction forces are reduced significantly. The approximations proposed in this paper are also applicable to the boundary element method. These procedures are an improvement over current methods and are applicable to both seismic excitations (S-waves, P-waves and surface waves) and externally applied transient loading.

Topographical and geological irregularities may induce large amplifications and significant spatial variations in seismic ground motion during earthquakes, consequently the site effects are very important in the consideration of the response of structures, such as dams, bridges, and life-line systems. This has motivated studies of more realistic problems of ground motion amplification by surface irregularities. Accurate prediction of ground motions requires three-dimensional analysis. Due to the complexity of three-dimensional surface irregularities, the available analytical methods for solving three-dimensional scattering and diffraction problems are limited and are applicable only to special geometries. The wave function expansion method^{13–16} is widely used, in which the unknown scattered wave field is expressed in terms of wave functions which satisfy the equation of motion, and radiation conditions at infinity. Traction-free boundary conditions are then imposed locally at several points on the surface of the cavity and the half-space.

Many numerical methods have been developed to solve realistic problems in strong ground motion seismology and earthquake engineering. The boundary integral equation methods (BIEMs) are very effective for studying the wave scattering in geotechnical problems involving unbounded domains. These methods require only discretization of the boundary of the scatterers and the radiation conditions at infinity can be modelled exactly,^{18–20} but they require evaluation of Green's functions which often require a large amount of computational effort and the methods are limited to problems involving linear materials.²¹ Finite element and finite-difference methods can be used to solve problems with complex geometries and non-linear materials, but these require the discretization of the entire domain of solution which makes such procedures inefficient for geotechnical problems. Many hybrid methods have been proposed which utilize the versatility of the finite-element and finite-difference methods for detailed modelling of the near field and the effectiveness of the BIEM and the wave function expansion techniques in the far field.^{22, 23}

The numerical procedure proposed in this paper can be used to analyze the scattering and diffraction of any elastic waves by three-dimensional surface irregularities, such as mountains, cavities and alluvial deposits with various shapes. The procedure can also be extended to consider similar problems which include hysteretic damping and nonlinearities in the soil properties.

2. EQUATION OF MOTION OF THE STRUCTURE

If both the seismic excitation and the externally applied transient loading are considered, the equation of motion of the structure in the time domain can be expressed as⁵

$$\begin{aligned} & \begin{bmatrix} \mathbf{M}_{ss} & \mathbf{M}_{sb} \\ \mathbf{M}_{bs} & \mathbf{M}_{bb} \end{bmatrix} \begin{Bmatrix} \ddot{\mathbf{u}}_s^t \\ \ddot{\mathbf{u}}_b^t \end{Bmatrix} + \begin{bmatrix} \mathbf{C}_{ss} & \mathbf{C}_{sb} \\ \mathbf{C}_{bs} & \mathbf{C}_{bb} \end{bmatrix} \begin{Bmatrix} \dot{\mathbf{u}}_s^t \\ \dot{\mathbf{u}}_b^t \end{Bmatrix} + \begin{bmatrix} \mathbf{K}_{ss} & \mathbf{K}_{sb} \\ \mathbf{K}_{bs} & \mathbf{K}_{bb} \end{bmatrix} \begin{Bmatrix} \mathbf{u}_s^t \\ \mathbf{u}_b^t \end{Bmatrix} \\ &= \begin{Bmatrix} 0 \\ -\mathbf{r}_b(t) \end{Bmatrix} + \begin{Bmatrix} \mathbf{p}_s(t) \\ \mathbf{p}_b(t) \end{Bmatrix} \end{aligned} \quad (1)$$

where \mathbf{M} is the mass matrix, \mathbf{K} is the stiffness matrix of the structure, \mathbf{u} , $\dot{\mathbf{u}}$, and $\ddot{\mathbf{u}}$ are the displacement, velocity and acceleration vectors, respectively, $\mathbf{r}_b(t)$ is the ground interaction force vector, and $\mathbf{p}(t)$ are externally applied force vectors. In equation (1), the subscripts b , and s denote the nodes on the soil–structure interface and the remaining nodes of the structure, respectively, and the superscript t denotes the total motion of the structure. The damping matrix \mathbf{C} represents viscous damping in the structure and is included for completeness but is not considered in the numerical examples presented later in this paper.

After the ground interaction force vector, $\mathbf{r}_b(t)$, is determined, the dynamic response of the structure can be obtained from equation (1) by using direct integration.

3. GROUND INTERACTION FORCE

In the substructure method, the ground interaction forces $\mathbf{r}_b(t)$ are given by the convolution integral,¹¹

$$\mathbf{r}_b(t) = \int_0^t \mathbf{M}_{bb}^g(t - \tau) (\ddot{\mathbf{u}}_b^t(\tau) - \ddot{\mathbf{u}}_b^g(\tau)) d\tau \quad (2)$$

where the superscript g denotes the unbounded soil with excavation, $\mathbf{M}_{bb}^g(t)$ is the acceleration unit-impulse response matrix and $\ddot{\mathbf{u}}_b^g(t)$ the acceleration vector, at the nodes b (which will subsequently lie on the structure–soil interface) of the soil with the excavation. Equation (2) can be used to calculate a general wave pattern consisting of oblique body waves and surface waves. The ground motion $\ddot{\mathbf{u}}_b^g(t)$, depends on the excavation so that it is more convenient to replace this generalized scattered motion by the free-field motion $\ddot{\mathbf{u}}_b^f(t)$, which does not depend on the excavation, with the exception of the location of the nodes for which it is to be calculated, and can be determined by the free-field site analysis.^{4,6}

The free-field system results when the excavated part of the soil is added to the soil with excavation as indicated in Figure 2. For this special case, the structure consists of the excavated part of the soil only, and part of the integral on the right-hand side of equation (2) can be reformulated by considering the equation of motion as⁵

$$\int_0^t \mathbf{M}_{bb}^g(t - \tau) \ddot{\mathbf{u}}_b^g(\tau) d\tau = \int_0^t \mathbf{M}_{bb}^f(t - \tau) \ddot{\mathbf{u}}_b^f(\tau) d\tau, \quad (3)$$

where \mathbf{M}_{bb}^f is the acceleration unit-impulse response matrix of the free-field site referred to the nodes at the soil–structure interface. To calculate the acceleration unit-impulse response matrix

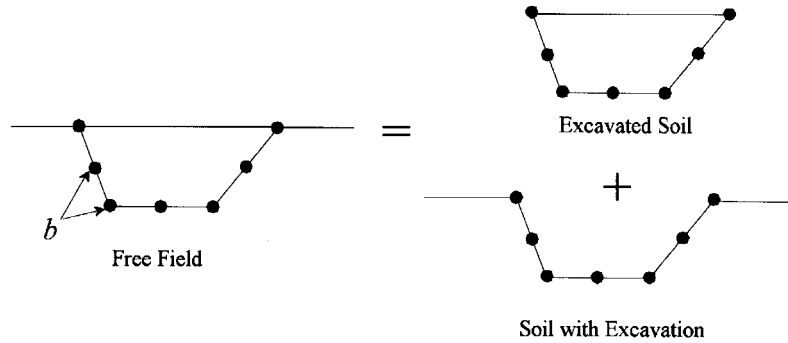


Figure 2. Free field site

of the free field site, the excavated part of the soil is discretized by the finite-element method. Standard finite-element discretization of the excavated part of the soil results in the acceleration unit-impulse response matrix \mathbf{M}^e of the excavated soil, which is given by

$$\mathbf{M}^e = -\frac{1 + 2\zeta i}{\omega^2} \mathbf{K}_e + \mathbf{M}_e \quad (4)$$

where \mathbf{K}_e is the stiffness matrix of the excavated soil, \mathbf{M}_e the mass matrix, ω the circular frequency, $i = \sqrt{-1}$ and ζ the hysteretic damping ratio of the excavated soil. The damping ratio is introduced for completeness, however, for the numerical results presented later, ζ is set to zero. The matrix \mathbf{M}^e can be decomposed into the submatrices \mathbf{M}_{ii} , \mathbf{M}_{ib} and \mathbf{M}_{bb} . The subscript b refers to the nodes on the structure-soil interface, and the subscript i refers to the remaining nodes. Eliminating the degree of freedom at i th node leads to

$$\mathbf{M}_{bb}^e = \mathbf{M}_{bb} - \mathbf{M}_{bi} \mathbf{M}_{ii}^{-1} \mathbf{M}_{ib} \quad (5)$$

where \mathbf{M}_{bb}^e denotes the acceleration unit-impulse response matrix of the excavated soil referred to the nodes b . Adding \mathbf{M}_{bb}^e to \mathbf{M}_{bb}^g results in the acceleration unit-impulse response matrix of the continuous soil (free-field site, see Figure 2) \mathbf{M}_{bb}^f , discretized at the same nodes b which subsequently lie on the structure-soil interface. That is

$$\mathbf{M}_{bb}^f = \mathbf{M}_{bb}^e + \mathbf{M}_{bb}^g \quad (6)$$

Substituting equations (6) and (3) into equation (2) gives

$$\mathbf{r}_b(t) = \mathbf{r}_b^{(1)}(t) + \mathbf{r}_b^{(2)}(t) \quad (7)$$

where

$$\begin{aligned} \mathbf{r}_b^{(1)}(t) &= \int_0^t \mathbf{M}_{bb}^g(t - \tau) (\ddot{\mathbf{u}}_b^t(\tau) - \ddot{\mathbf{u}}_b^f(\tau)) d\tau \\ \mathbf{r}_b^{(2)}(t) &= - \int_0^t \mathbf{M}_{bb}^e(t - \tau) \ddot{\mathbf{u}}_b^f(\tau) d\tau \end{aligned}$$

The acceleration unit-impulse response matrix $\mathbf{M}_{bb}^g(t)$ is calculated using the scaled boundary finite-element method.¹¹ It may be shown that

$$\mathbf{r}_b^{(2)}(t) = -F^{-1}[\mathbf{M}_{bb}^g(\omega)\ddot{\mathbf{u}}_b^f(\omega)] \quad (8)$$

where $F^{-1}[*]$ denotes the Inverse Fourier Transformation. The term enclosed in square bracket on the right-hand side of equation (8) is evaluated in the frequency domain and then transformed to the time domain as indicated.

Substituting equation (7) into the equation of motion of structure (1) enables the response of this structure-soil system to the incident wave and/or applied transient loading to be determined by a numerical integration scheme in the time domain.

4. APPROXIMATIONS IN TIME AND SPACE

The scaled boundary finite-element method is a rigorous method for modelling the unbounded media. Since the exact unit-impulse response matrix of an unbounded medium is fully coupled in both space and time, its calculation using the scaled boundary finite-element method requires considerable computational effort, however the result is very accurate. In engineering practice, it is desirable to reduce computational effort by introducing approximations in both time and space. The proposed procedures in this paper significantly reduce the computational time with little loss of accuracy.

4.1. Approximation in time

The acceleration unit-impulse response matrix, $\mathbf{M}_{bb}^g(t)$, can be decomposed as (see Figure 3)¹¹

$$\mathbf{M}_{bb}^g(t) = \mathbf{C}\mathbf{H}(t) + \mathbf{K}tH(t) + \mathbf{M}_f(t) \quad (9)$$

where \mathbf{K} is the static-stiffness matrix, \mathbf{C} is the matrix of dashpot coefficients at circular frequency $\omega = 0$ of the unbounded soil, $H(t)$ is the Heaviside-step function, and $\mathbf{M}_f(t \rightarrow \infty) = 0$. It follows that the acceleration unit-impulse matrix, which is non-linear with respect to time, can be approximated as a piece-wise linear function of time and usually only few linear segments, four or five, are adequate. In this paper, the unit-impulse matrix is approximated by a few linear segments before time t_k and one linear segment after time t_k . Here t_k can be determined by balancing the accuracy requirement and the computational effort required for calculation of the acceleration unit-impulse response matrix.

The scaled boundary finite-element method is used to calculate the acceleration unit-impulse response matrix, which results in a special type of integral equation. In this study, the time discretization scheme proposed by Wolf and Song¹¹ is used to solve the scaled boundary finite-element equation, in which the response matrix is assumed to be piece-wise constant over each time step. This scheme is a conditionally stable scheme and the time step used must be less than the critical step size to obtain a stable solution, which requires significant computational effort.

As already mentioned, the response matrix is approximated by a few linear segments, therefore it is only necessary to calculate the response matrix at these time steps. The time discretization scheme used is a conditionally stable scheme, consequently the solution will become unstable after a couple of time steps if the time steps used are too large. To estimate the stability of the time

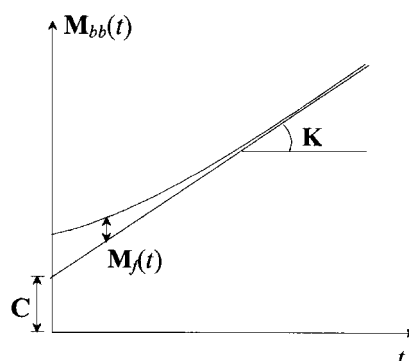


Figure 3. Decomposition of the acceleration unit-impulse response matrix

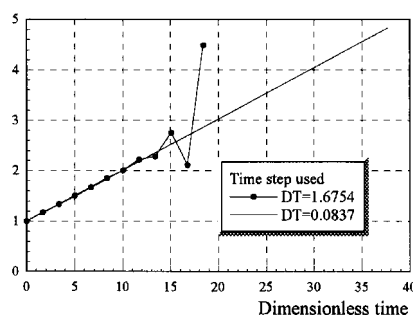


Figure 4. Dimensionless unit-impulse response coefficient, $E(t)/E(0)$, of the hemispherical cavity described in Section 6.2 versus dimensionless time. $E(t)$ is the summation of all elements of the unit-impulse response matrix at time t and $E(0) = E(t = 0)$

discretization scheme, the acceleration unit-impulse response matrices of the hemispherical cavity described in Section 6.2 are calculated by using different time steps, and the results are compared in Figure 4. This numerical study shows that although a very large time step is used, satisfactory solutions are still obtained within the first several time steps, say five or six. In the numerical examples presented later in this paper, the time step is chosen as $t_k/5$, and only five time steps are used to calculate the acceleration unit-impulse response matrix before time $t = t_k$. The computational effort is further reduced significantly, see Figure 5(b).

To obtain sufficient accuracy in the interested frequency range, the size of linear segments, $\Delta t'$, must satisfy

$$\Delta t' \leq \frac{\omega_{\max}}{\pi} \quad (10)$$

where ω_{\max} is the maximum circular frequency of the interested frequency range. Meanwhile, t_k should also be chosen carefully to ensure the desired accuracy.

4.2. Approximation in space

Approximation in space is another approach to reduce the computational effort required for the calculation of the unit-impulse response matrices and the ground interaction force.

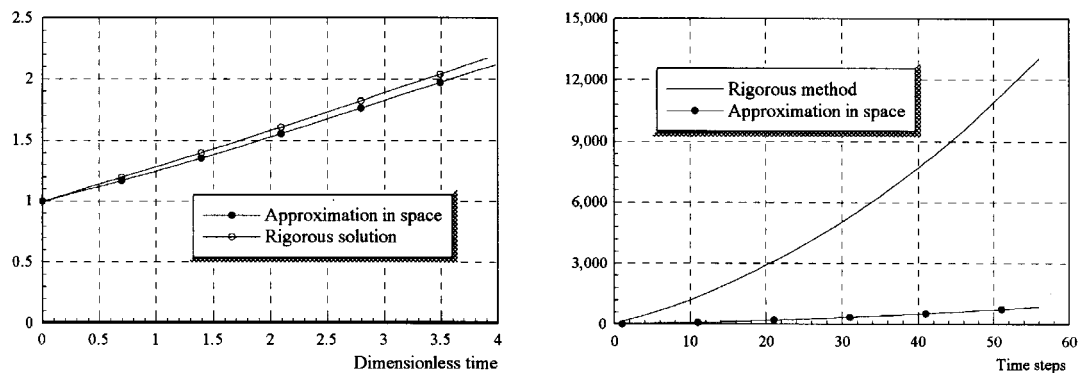


Figure 5. (a) Dimensionless unit-impulse response coefficients, $E(t)/E(0)$, of the hemi-spherical cavity versus dimensionless time. $E(t)$ is the summation of all elements of the unit-impulse response matrix at time t and $E(0) = E(t = 0)$; (b) Computation CPU time (s) required for the calculation

The basic equation of the scaled boundary finite-element method in the time domain is a integral equation with respect to a unknown unit-impulse response matrix of order N and the linear algebra package LAPACK is used to solve the equation. Computational effort for most LAPACK driver routines is proportional to N^3 ,²⁴ consequently if the basic equation of the scaled boundary finite-element method is reduced to M equations with the unknown matrix of order K ($N/M < K < N$) by introducing approximations, the computational effort for solving these M integral equations is much less than that for solving the original equation.

In the scaled boundary finite-element method, the structure-soil interface is treated as only one substructure so that the unit-impulse response matrix is a full matrix. To introduce approximation in space, the structure-soil interface is divided into several substructures and the unit-impulse response matrices for the substructures are calculated first and then assembled to form the global unit-impulse response matrix for the structure-soil interface, as in the standard finite-element method. This process is equivalent to reducing the basic equation of the scaled boundary finite-element method to M integral equations with the unknown matrix of order K . The computational effort for solving each equation is proportional to K^3 , so that the total computational effort for the new scheme will be proportional to $K^3 M$. Consequently, the computational effort will be reduced by a factor of $L = N^3/(K^3 M)$ ($M < L < M^2$) by introducing the approximation in space. Actually, this factor is much greater than L , see Figure 5(b).

The unit-impulse response matrix will be a sparse matrix if the degrees of freedom are properly numbered within every substructure, so that the computational effort for the calculation of both the unit-impulse response matrices and the ground interaction forces will be reduced significantly. Furthermore, the scaling centre (similarity centre) can be chosen for each substructure independently if necessary.

To assess the accuracy and efficiency of the proposed approximation in space, the acceleration unit-impulse response matrices of the hemi-spherical cavity described in Section 6.2 are calculated by introducing the approximation in space. The soil-structure interface is divided into four substructures; every substructure consists of a quarter of the interface. In this example, $N = 435$, $M = 4$, $K = 129$ (see Section 6.2), so that the computational effort is reduced by a factor of 10 by introducing the approximation in space. Figure 5(a) compares the dimensionless

unit-impulse response coefficients of the hemispherical cavity calculated by introducing approximation in space with those obtained by the rigorous method. The computation time required for the calculation of the acceleration unit-impulse response matrices are presented in Figure 5(b). The computer used in the calculation is Pentium II 300 Hz. Figure 5(b) shows that the CPU time used for this example is reduced from that for the rigorous method by a factor of 15 by dividing the soil-structure interface into four substructures. It can be concluded from this numerical study that the accuracy of the proposed approximation in space is satisfactory while the computational effort required is reduced significantly.

5. TIME INTEGRATION

Implicit integration schemes, which ensure numerical stability, are presented. To obtain the solution at time $t + \Delta t$, the equation of motion of structure is considered at time $t + \Delta t$,

$$\begin{aligned} & \begin{bmatrix} \mathbf{M}_{ss} & \mathbf{M}_{sb} \\ \mathbf{M}_{bs} & \mathbf{M}_{bb} \end{bmatrix} \begin{Bmatrix} {}^{n+1}\ddot{\mathbf{u}}_s^t \\ {}^{n+1}\ddot{\mathbf{u}}_b^t \end{Bmatrix} + \begin{bmatrix} \mathbf{C}_{ss} & \mathbf{C}_{sb} \\ \mathbf{C}_{bs} & \mathbf{C}_{bb} \end{bmatrix} \begin{Bmatrix} {}^{n+1}\dot{\mathbf{u}}_s^t \\ {}^{n+1}\dot{\mathbf{u}}_b^t \end{Bmatrix} + \begin{bmatrix} \mathbf{K}_{ss} & \mathbf{K}_{sb} \\ \mathbf{K}_{bs} & \mathbf{K}_{bb} \end{bmatrix} \begin{Bmatrix} {}^{n+1}\mathbf{u}_s^t \\ {}^{n+1}\mathbf{u}_b^t \end{Bmatrix} \\ & = \begin{Bmatrix} 0 \\ -{}^{n+1}\mathbf{r}_b \end{Bmatrix} + \begin{Bmatrix} {}^{n+1}\mathbf{p}_s \\ {}^{n+1}\mathbf{p}_b \end{Bmatrix} \end{aligned} \quad (11)$$

where the superscript $n + 1$ denotes 'at time $(n + 1)\Delta t$ ', consequently ${}^{n+1}\ddot{\mathbf{u}}_s^t = \ddot{\mathbf{u}}_s^t((n + 1)\Delta t)$.

Numerical evaluation of the convolution integrals in the calculation of the ground interaction forces is the most computationally expensive part of a soil-structure interaction analysis, consequently it is desirable to reduce the computational effort required. A significant effort has been made in linear system theory and dynamic soil-structure interaction analysis, and several efficient schemes have been developed for numerical evaluation of convolution integrals.²⁵ Based on the aforementioned approximation in time, a very efficient new scheme is developed in this paper for numerical evaluation of the convolution integrals in the calculation of the ground interaction forces. The basic approximations for the new scheme are:

1. The unit-impulse matrix is approximated by a few linear segments before time t_k and one linear segment after time t_k .
2. The acceleration is approximated as linear over each time step.
3. The time steps for the convolution integrals are the same as for the time integrations.

To evaluate the ground interaction forces at time $t + \Delta t$, the time interval 0 to $t + \Delta t$, where $t = n\Delta t$ and Δt is the time step for the time integration, is divided into $M \leq t_k/\Delta t'$ subintervals with size $\Delta t' = N\Delta t$, and $K = (t + \Delta t - M\Delta t')/\Delta t$ subintervals with size Δt . For computational convenience, N , K , and M are taken as integers. The first term of the ground interaction forces for time $t + \Delta t$ is given by

$$\begin{aligned} \mathbf{r}_b^{(1)}(t + \Delta t) &= \sum_{i=1}^M \int_{(i-1)\Delta t'}^{i\Delta t'} \mathbf{M}_{bb}^g(\tau) \Delta \ddot{\mathbf{u}}_b(t + \Delta t - \tau) d\tau \\ &+ \sum_{i=1}^K \int_{MN\Delta t + (i-1)\Delta t}^{MN\Delta t + i\Delta t} \mathbf{M}_{bb}^g(\tau) \Delta \ddot{\mathbf{u}}_b(t + \Delta t - \tau) d\tau \end{aligned} \quad (12)$$

where $\Delta \ddot{\mathbf{u}}_b(t + \Delta t - \tau) = \ddot{\mathbf{u}}_b^t(t + \Delta t - \tau) - \ddot{\mathbf{u}}_b^f(t + \Delta t - \tau)$.

According to approximations 1 and 2, the first term on the right-hand side of equation (12) can be evaluated as

$$\begin{aligned} & \sum_{i=1}^M \int_{(i-1)\Delta t}^{i\Delta t} \mathbf{M}_{bb}^g(\tau) \Delta \ddot{\mathbf{u}}_b(t + \Delta t - \tau) d\tau \\ &= \sum_{i=1}^M (i-1)^N \mathbf{M}_{bb}^g [\alpha_1 \Delta^{n+1-(i-1)N} \ddot{\mathbf{u}}_b + \alpha_2 \Delta^{n+1-iN} \ddot{\mathbf{u}}_b + \sum_{j=1}^{N-1} \alpha_3 \Delta^{n+1-(i-1)N-j} \ddot{\mathbf{u}}_b] \\ & \quad + \sum_{i=1}^M {}^{iN} \mathbf{M}_{bb}^g [\alpha_2 \Delta^{n+1-(i-1)N} \ddot{\mathbf{u}}_b + \alpha_1 \Delta^{n+1-iN} \ddot{\mathbf{u}}_b + \sum_{j=1}^{N-1} \alpha_4 \Delta^{n+1-(i-1)N-j} \ddot{\mathbf{u}}_b] \end{aligned} \quad (13)$$

where $\alpha_1 = (\Delta t/6N)(3N-1)$, $\alpha_2 = \Delta t/6N$, $\alpha_3 = \Delta t(1-j/N)$, and $\alpha_4 = \Delta t(j/N)$. In (13) the left superscript ‘ iN ’ denotes ‘evaluated at time $iN\Delta t$ ’, consequently ${}^{iN} \mathbf{M}_{bb}^g = \mathbf{M}_{bb}^g(iN\Delta t)$ and $\Delta^{n+1-iN} \ddot{\mathbf{u}}_b = \Delta \ddot{\mathbf{u}}_b((n+1-iN)\Delta t)$.

Because different approximations are used for the case $t + \Delta t \leq t_k$ and the case $t + \Delta t > t_k$, the second term on the right-hand side of equation (12) should be evaluated for these two cases. For the case $t + \Delta t \leq t_k$, the second term on the right-hand side of equation (12) is evaluated as

$$\begin{aligned} & \sum_{i=1}^K \int_{MN\Delta t + (i-1)\Delta t}^{MN\Delta t + i\Delta t} \mathbf{M}_{bb}^g(\tau) \Delta \ddot{\mathbf{u}}_b(t + \Delta t - \tau) d\tau \\ &= {}^{MN} \mathbf{M}_{bb}^g [\alpha_1 \Delta^{n+1-MN} \ddot{\mathbf{u}}_b + \alpha_5 \Delta^{n+1-MN-K} \ddot{\mathbf{u}}_b + \sum_{j=1}^{K-1} \alpha_3 \Delta^{n+1-MN-j} \ddot{\mathbf{u}}_b] \\ & \quad + {}^{(M+1)N} \mathbf{M}_{bb}^g [\alpha_2 \Delta^{n+1-MN} \ddot{\mathbf{u}}_b + \alpha_6 \Delta^{n+1-MN-K} \ddot{\mathbf{u}}_b + \sum_{j=1}^{K-1} \alpha_4 \Delta^{n+1-MN-j} \ddot{\mathbf{u}}_b] \end{aligned} \quad (14)$$

where $\alpha_5 = (\Delta t/6N)(3N-3K+1)$, $\alpha_6 = (\Delta t/6N)(3K-1)$.

For the case $t + \Delta t > t_k$, the acceleration unit-impulse response matrix at time $\tau > MN\Delta t$, $\mathbf{M}_{bb}^g(\tau)$, is calculated by extrapolating matrices ${}^{MN} \mathbf{M}_{bb}^g$ and ${}^{(M-1)N} \mathbf{M}_{bb}^g$, consequently the second term on the right-hand side of equation (12) is evaluated as

$$\begin{aligned} & \sum_{i=1}^K \int_{MN\Delta t + (i-1)\Delta t}^{MN\Delta t + i\Delta t} \mathbf{M}_{bb}^g(\tau) \Delta \ddot{\mathbf{u}}_b(t + \Delta t - \tau) d\tau \\ &= {}^{MN} \mathbf{M}_{bb}^g (\alpha_7 \Delta^K \ddot{\mathbf{u}}_b + \sum_{i=1}^{K-1} \alpha_9 \Delta^{n+1-MN-i} \ddot{\mathbf{u}}_b) \\ & \quad - {}^{(M-1)N} \mathbf{M}_{bb}^g (\alpha_8 \Delta^K \ddot{\mathbf{u}}_b + \sum_{i=1}^{K-1} \alpha_{10} \Delta^{n+1-MN-i} \ddot{\mathbf{u}}_b) \end{aligned} \quad (15)$$

where $\alpha_7 = (\Delta t/6N)(3N+1)$, $\alpha_8 = \Delta t/6N$, $\alpha_9 = (1+i/N)\Delta t$, and $\alpha_{10} = (i/N)\Delta t$.

Substituting equations (13), (14) and (15) into equation (12) leads to a very efficient scheme for calculation of the ground interaction forces. Numerical evaluation of equation (12) only requires $2(M+1)$ matrix vector multiplications and about $2M(N+1) + 2K$ vector summations, where M is usually equal to four or five. A matrix vector multiplication requires L^2 , where L is the order of the matrix and the vector, scalar multiplications and L^2 scalar summations, therefore matrix

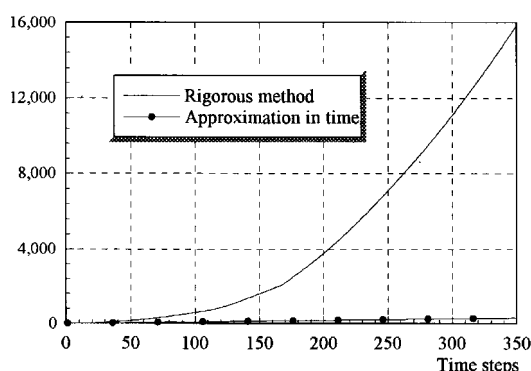


Figure 6. Computation CPU time required for numerical evaluation of convolution integrals by using different methods

vector multiplications are numerically intensive tasks. Usually, a few linear segments, four or five, are adequate to approximate the acceleration unit-impulse response matrix, consequently the numerical scheme developed here significantly reduces the computational effort required for numerical evaluation of the convolution integrals in the calculation of the ground interaction forces for earthquake engineering problems.

Substituting (12) and (7) into (11) gives the equation of motion of structure at time $t + \Delta t$, which can be solved by using the Newmark method or Wilson- θ method.¹² To illustrate the efficiency of the proposed scheme, Figure 6 compares the computation CPU time required for numerical evaluation of convolution integrals in the calculation of the ground interaction forces for the hemispherical cavity described in Section 6.2. In this example, the acceleration unit-impulse response matrix is approximated by five linear segments before dimensionless time $\bar{t}_k = 10.47$, and approximated as a linear function of time after time \bar{t}_k . Figure 6 shows that the scheme proposed in this paper for numerical evaluation of convolution integrals is very efficient.

6. NUMERICAL EXAMPLES

The procedure proposed in this paper can be used in the analysis of dynamic soil-structure interaction and wave scattering by three-dimensional surface irregularities. Seismic excitations and externally applied transient loadings can be included in analysis.

6.1. Spherical cavity embedded in full-space

As a check on the new scheme, a spherical cavity embedded in a full-space is analysed and subjected to a spatially uniform application of pressure. This is a one spatial dimensional problem and its analytical solution is available.¹¹ The following pressure pulse is applied in the radial direction to the wall of the cavity with $t_0 = 3.46r_0/c_p$,

$$p(t) = \begin{cases} \frac{p_0}{2} \left(1 - \cos \frac{2\pi t}{t_0} \right), & 0 \leq t \leq t_0 \\ 0, & t < 0, t > t_0 \end{cases} \quad (16)$$

where r_0 is the radius of the cavity and c_p the speed of the dilatational wave.

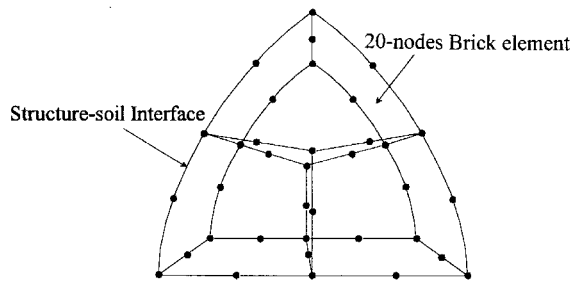


Figure 7. Finite-element mesh of the spherical cavity embedded in full-space

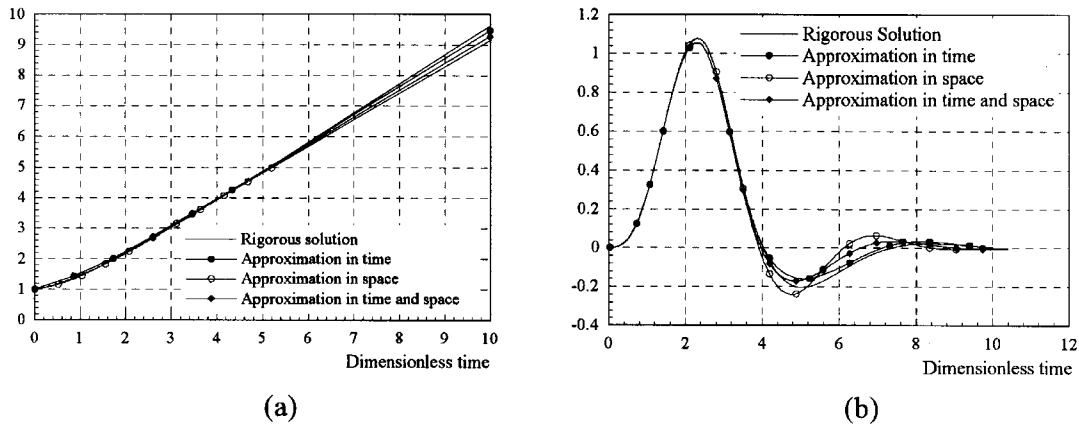


Figure 8. (a) Dimensionless acceleration unit-impulse response coefficient, $E(t)/E(0)$, of the spherical cavity embedded in full-space versus dimensionless time. $E(t)$ is the summation of all elements of the unit-impulse response matrix at time t and $E(0) = E(t = 0)$; (b) Dimensionless displacement response of the spherical cavity

Due to symmetry, only one octant of the cavity is modelled. A portion of the soil adjacent to the wall is treated as the structure and discretized by three 20-node brick elements with $3 \times 3 \times 3$ Gaussian integration (Figure 7) and the structure-soil interface is discretized by three eight-node isoparametric interface elements with 3×3 Gaussian integration. To compare with available results, the dimensionless time \bar{t} is defined by $\bar{t} = t c_p / r_0$, and the dimensionless displacement $\bar{u}(\bar{t})$ is defined by $\bar{u}(\bar{t}) = u_0(\bar{t}) K^\infty / 4\pi r_0^2 p_0$, where $K^\infty = 16\pi G r_0$ is the static-stiffness coefficient.

This example is analysed for four different cases: rigorous case without approximation, approximation in time only, approximation in space only, and approximation in both space and time. For the case of approximation in time, the acceleration unit-impulse response matrix is approximated by five linear segments before dimensionless time $\bar{t}_k = 5.2$, and approximated as a linear function of time after \bar{t}_k . For the case of approximation in space, the soil-structure interface is divided into three substructures, with only one element in every substructure. This is the extreme case, and will lead to the worst results among all possible approximations in space. This case can be used to assess critically the accuracy of the approximation in space proposed in this paper. Figures 8(a) and 8(b) present the dimensionless acceleration unit-impulse response

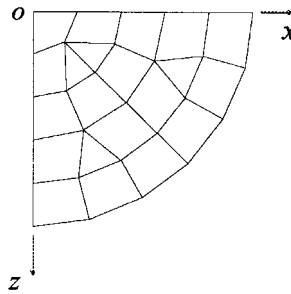


Figure 9. A cross-section of the finite-element mesh

coefficients and the dimensionless displacement response of the spherical cavity embedded in full-space for these four different cases. For the extreme case of approximation in space, excellent results are still achieved within the loading duration ($\bar{t} \leq 3.46$). After time $\bar{t} = 3.46$, the vibration of the system is a free vibration, which is usually of no interest in earthquake engineering.

6.2. Wave scattering by hemi-spherical cavities

To compare with existing analytical results, the scattering of plane harmonic waves by hemi-spherical cavities in the homogeneous elastic half-space is analysed. The dimensionless frequencies, η_s and η_p , are defined throughout the following sections as

$$\eta_s = \frac{2R}{\lambda_s}, \quad \eta_p = \frac{2R}{\lambda_p}$$

where λ_p is the wavelength of the dilatational wave, λ_s is the wavelength of the shear wave, and $2R$ is the maximum width of a cross-section of the surface irregularities, which lie in the x - z plane passing through the centre of the surface irregularities. The scattering motion depends on the dimensionless frequencies and Poisson's ratio ν .

In the present analysis, two groups of elements are used, one is used to discretize the structural-soil interface (the surface of the cavity in this case), while the other is used to discretize the excavated soil (hemi-sphere) which will form the half-space together with the structure-soil interface to determine the seismic free-field input motion (see Figure 2). The finite-element model is generated by rotating Figure 9, 360° about the z -axis in 15° increments. The model consists of 534 nodes, 504 eight-node three-dimensional elements for the excavated soil and 144 four-node two-dimensional elements for the soil-structure interface.

To investigate the efficiency and accuracy of the proposed approximation in space, two finite-element models are used to idealize the soil-structure interface and no approximation is introduced in time. In the first model, the whole interface is treated as one substructure so that there are 144 four-node two-dimensional elements and 145 nodes on the soil-structure interface, and the unit-impulse response matrix will be a full-square matrix of order 435. In the second model, the interface is divided into four substructures; every substructure consists of a quarter of the interface. Point o is chosen as the similarity centre for all four substructures. There are 36 four-node two-dimensional elements and 43 nodes in every substructure so that the unit-impulse response matrix for every substructure will be a full-matrix of order 129 and the unit-impulse

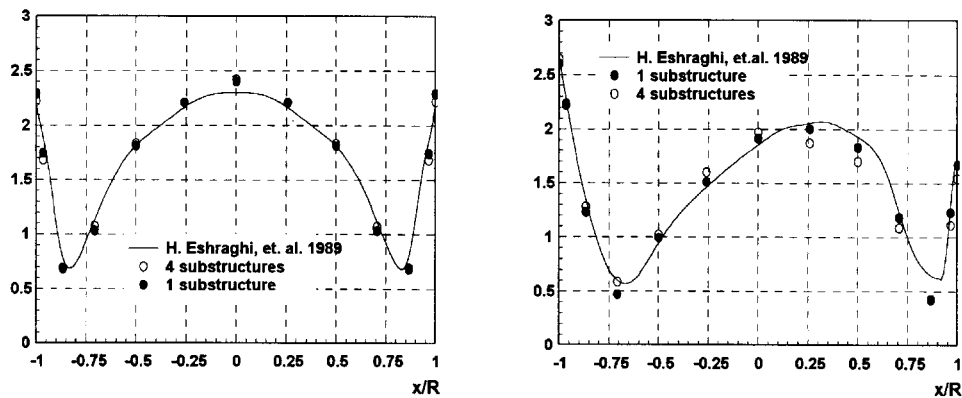


Figure 10. Amplitudes of the y-component of the surface displacement at the stations along the x-axis for the incident SH waves at angles of incidence of 90 and 60°. Dimensionless frequency $\eta_s = 0.75$, and Poisson's ratio $\nu = 1/3$

response matrix of the whole soil–structure interface will be a highly sparse matrix. According to the analysis in Section 4.2, the computational effort is reduced from that for the rigorous method by a factor of about 10 in this case. Actually, this factor is about 15, see Figure 5(b).

In this numerical example, no structure is actually introduced into the soil–structure interaction system, so the ground interaction force is directly applied to the surface of the cavity. The dimensionless time steps \bar{t} ($\bar{t} = t\pi c_s/R$) for both the time integration and the calculation of the unit-impulse response matrix are all set to 0.0697. Figure 10 shows the amplitudes of the y-component of the surface displacement at stations along the x-axis for the incident SH waves at angles of incidence of 90 and 60° measured from the horizontal to the direction of incidence for dimensionless frequency $\eta_s = 0.75$ and Poisson's ratio $\nu = 1/3$. The control point is chosen at point *o* and the control motion is the harmonic motion with amplitude of 2 which corresponds to a unit-amplitude incident SH wave. It can be concluded from these results that the approximations in space lead to little accuracy loss while reducing the computational effort required significantly, so that the approximation schemes are very attractive for engineering problems.

To estimate the scattering motion on the surface of the cavity and half-space, another different finite-element model is used, in which a portion of soil adjacent to the surface of the cavity is treated as structure and discretized by eight-node brick elements. The finite-element model for a hemi-spherical cavity is generated by rotating Figure 11, 360° about z-axis in 11.25° increments. The model consists of 1030 nodes, 512 eight-node brick elements for structure and 480 eight-node brick elements for the excavated soil. The soil–structure interface is divided into four substructures and each substructure consists of a quarter of the interface and modelled by 64 four-node 2-D elements. The acceleration unit-impulse response matrix is a sparse matrix and is approximated as a piece-wise linear function of time before dimensionless time $\bar{t}_k = 8.377$ ($\bar{t}_k = t_k\pi c_p/R$) and a linear function of time after \bar{t}_k . Only four linear segments are used to approximate the acceleration unit-impulse response matrix before time \bar{t}_k .

Figure 12 shows the dimensionless surface amplitudes of vertical and horizontal displacements of a hemi-spherical cavity at stations along the x-axis for incident P wave at angle of incidence of 90 and 60°, for the dimensionless frequency $\eta_p = 0.25$, and 0.5, respectively. Figure 13 shows the dimensionless surface amplitudes of vertical and horizontal displacements of the hemi-spherical

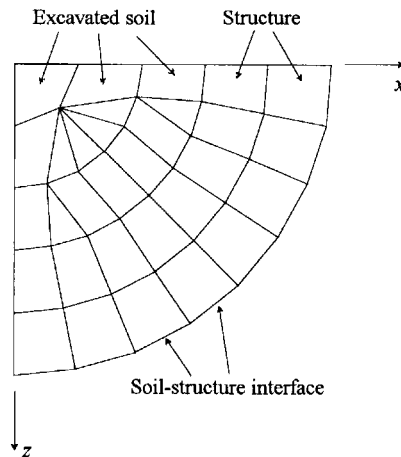


Figure 11. A cross-section of the finite-element model

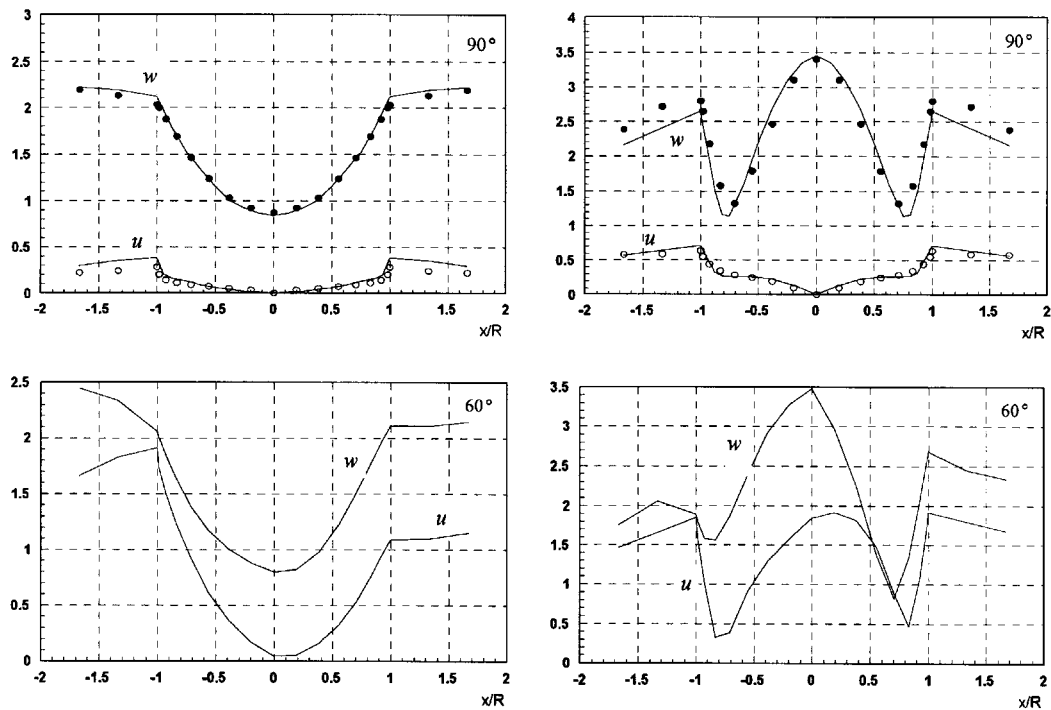


Figure 12. Surface amplitudes of a hemi-spherical cavity for incident P wave at angle of incidence of 90 and 60° respectively. Dimensionless frequency $\eta_p = 0.25$, and 0.5. Poisson's ratio $\nu = 0.25$. Circles and dots correspond to the results obtained by the present method, while solid lines correspond to the results obtained by Sanchez-Sesma¹⁴

cavity at stations along x -axis for vertically incident SV wave, for the dimensionless frequency $\eta_s = 0.75$. Note that for a half-space, displacements would be vertical with amplitude of two for a vertically incident P wave, and horizontal with amplitude of two for a vertically incident SV wave.

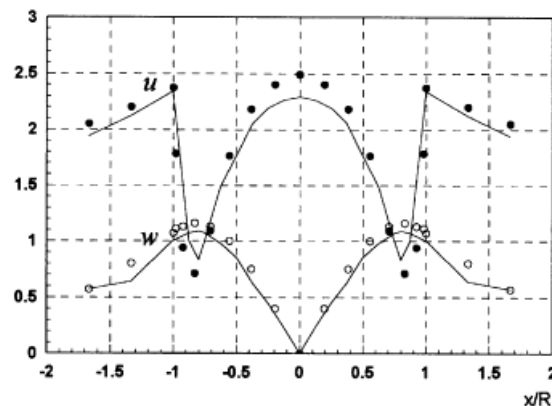


Figure 13. Surface amplitudes of a hemi-spherical cavity for vertically incident SV wave. Dimensionless frequency $\eta_s = 0.75$. Poisson's ratio $\nu = 0.333$. Circles and dots correspond to the results obtained by the present method, while solid lines correspond to the results obtained by Eshraghi¹⁵

Numerical results for incident waves with low frequency, say $\eta_p \leq 0.5$, are in good agreement with those obtained from the wave expansion function method.¹⁴ However, accuracy of the numerical results decreases with the increase in the value of η_p . Thus the approximations proposed are suitable for problems with low frequency. Because the frequency range involved in earthquake engineering is usually below $\eta_p = 0.5$, this restriction does not prevent the application of the new scheme to earthquake engineering problems. For higher frequency problems, a finer finite-element model must be used and the acceleration unit-impulse response matrix should be approximated by linear segments with smaller size. This will significantly increase the computational effort required.

6.3. Wave scattering by cubic cavity

Due to the complexity of three-dimensional surface irregularities, analytical methods are only applicable for some special geometries, such as a hemi-sphere or a semi-ellipsoid. However, wave scattering and diffraction by other kind of three-dimensional surface irregularities are of interest in earthquake engineering studies. For example, foundations are a common type of three-dimensional surface irregularities in civil engineering and earthquake engineering. The wave scattering and diffraction by this type of surface irregularities are very difficult to obtain by analytical methods, and no comparable results are available. The new scheme proposed in this study can be used to study the scattering and diffraction of seismic waves by any realistic three-dimensional surface irregularities. As an example, the scattering of SH-, SV- and P-waves by a cubic cavity, representing the excavation for a foundation, are studied in detail (Figure 14).

In this study, no structure exists and only the surface of the cavity needs to be modelled. The soil-structure interface is modelled by five substructures and each of them is idealized by 64 four-node two-dimensional elements and consists of 81 nodes. Figure 15 shows the surface amplitudes of the cavity at stations along the x -axis for incident P-, SH-, and SV-waves at angles of incidence of 90 and 60° measured from the horizontal to the direction of incidence. In Figure 15, l is measured along the surface of the cavity.

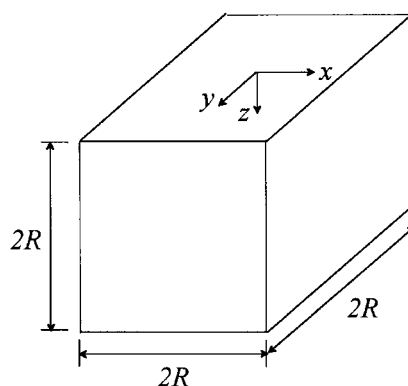


Figure 14. A cubic cavity

6.4. Wave scattering by hemi-spherical alluvial deposit

Material properties for the deposit R and the half-space E are assumed to be related by $G^R = 0.3G^E$ and $\rho^R = 0.6\rho^E$, where G is shear modulus and ρ is density, with Poisson's ratio $\nu^R = 0.3$ and $\nu^E = 0.25$, respectively.

The finite-element model used here is similar to that shown in Figure 11. The model consists of 1030 nodes, 992 eight-node brick elements for both excavated soil and structure. The soil-structure interface is divided into four substructures consequently the acceleration unit-impulse response matrix is a sparse matrix. The approximations used for the unit-impulse response matrix are the same as Section 6.2. Figure 16 presents the surface amplitudes of vertical and horizontal displacements at stations along the x -axis for incident P-, SV- and SH-waves at angle of incidence of 90° and 60° with a dimensionless frequency $\eta_p = 0.5$, respectively.

6.5. Wave scattering by cubic alluvial deposit

As already noted, foundations are a common type of a three-dimensional surface irregularity and wave scattering and diffraction by foundations are of interest in earthquake engineering studies. Consequently, wave scattering and diffraction by a cubic alluvial deposit are studied. Material properties for the deposit R and the half-space E are assumed to be the same as Section 6.4 and the finite-element model is similar to Section 6.3.

Figure 17 shows the surface amplitudes of the cubic alluvial deposit at stations along the x -axis for incident P-, SH-, and SV- waves at angle of incidence of 90° and 60° measured from the horizontal to the direction of incidence, respectively.

6.6. Wave scattering by semicylindrical deposit

The wave scattering by a semicylindrical deposit is studied and the results are compared with those obtained by two dimensional analysis.¹⁷ To compare with the results obtained by two-dimensional analysis, the model is assumed to be of the plane strain type by eliminating all degrees of freedom in y -direction. The soil-structure interface is divided into six substructures and

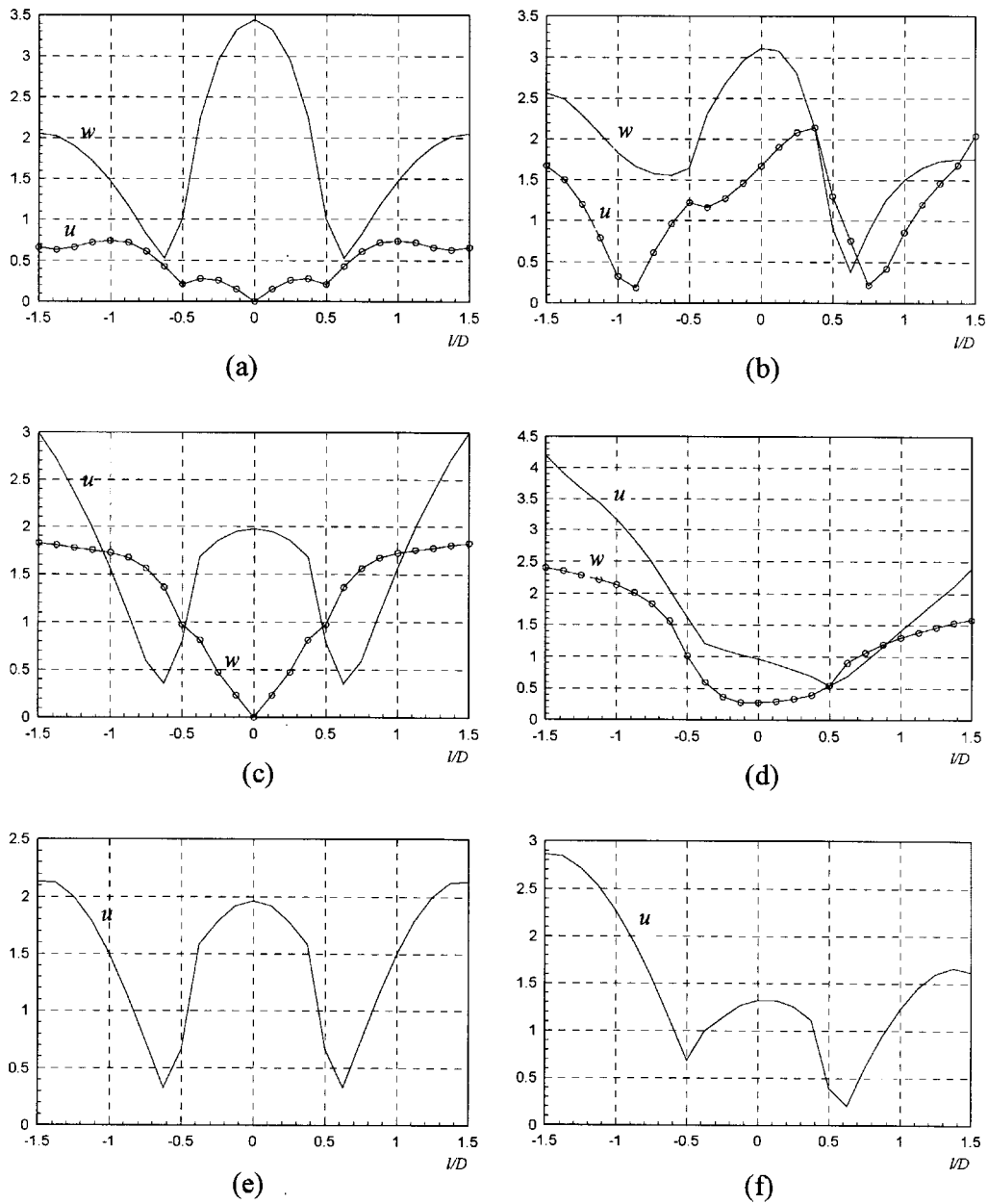


Figure 15. Surface amplitudes of a cubic cavity for incident waves at angle of incidence of 90° and 60° respectively. Poisson's ratio $\nu = 0.25$ (a) and (b) P-wave, dimensionless frequency $\eta_p = 0.25$; (c) and (e) SV-wave, dimensionless frequency $\eta_s = 0.25$; (d) and (f) SH-wave, dimensionless frequency $\eta_s = 0.25$

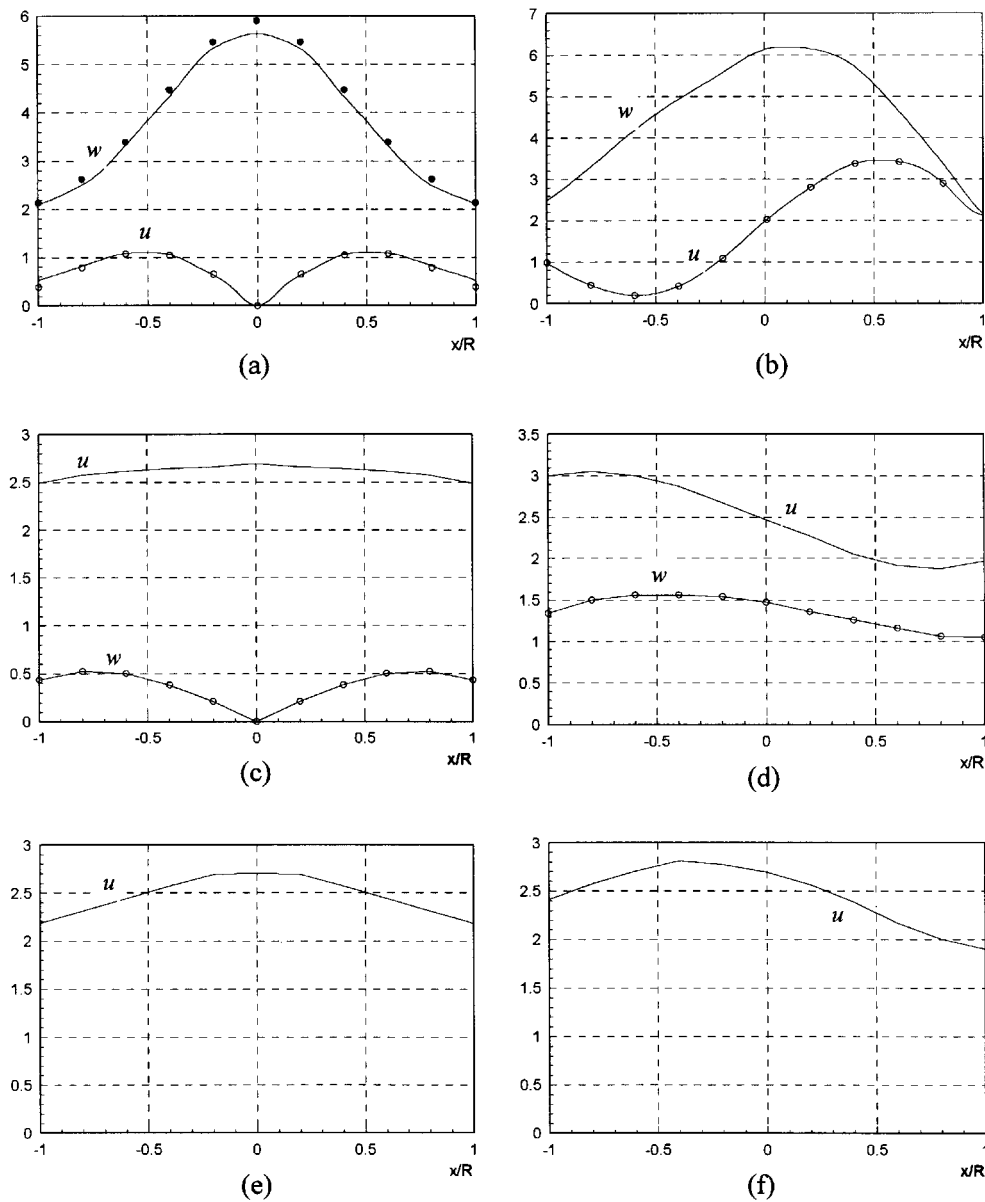


Figure 16. Surface amplitudes of a hemi-spherical deposit for incident waves at angle of incidence of 90 and 60° (a) and (b) P-waves. Dimensionless frequency $\eta_p = 0.5$; (c) and (d): SV-waves. Dimensionless frequency $\eta_s = 0.5$; (e) and (f) SH-waves. Dimensionless frequency $\eta_s = 0.5$. In (a), circles and dots correspond to the results obtained by the present method, while solid lines correspond to the results obtained Sanchez-Sesma¹⁴

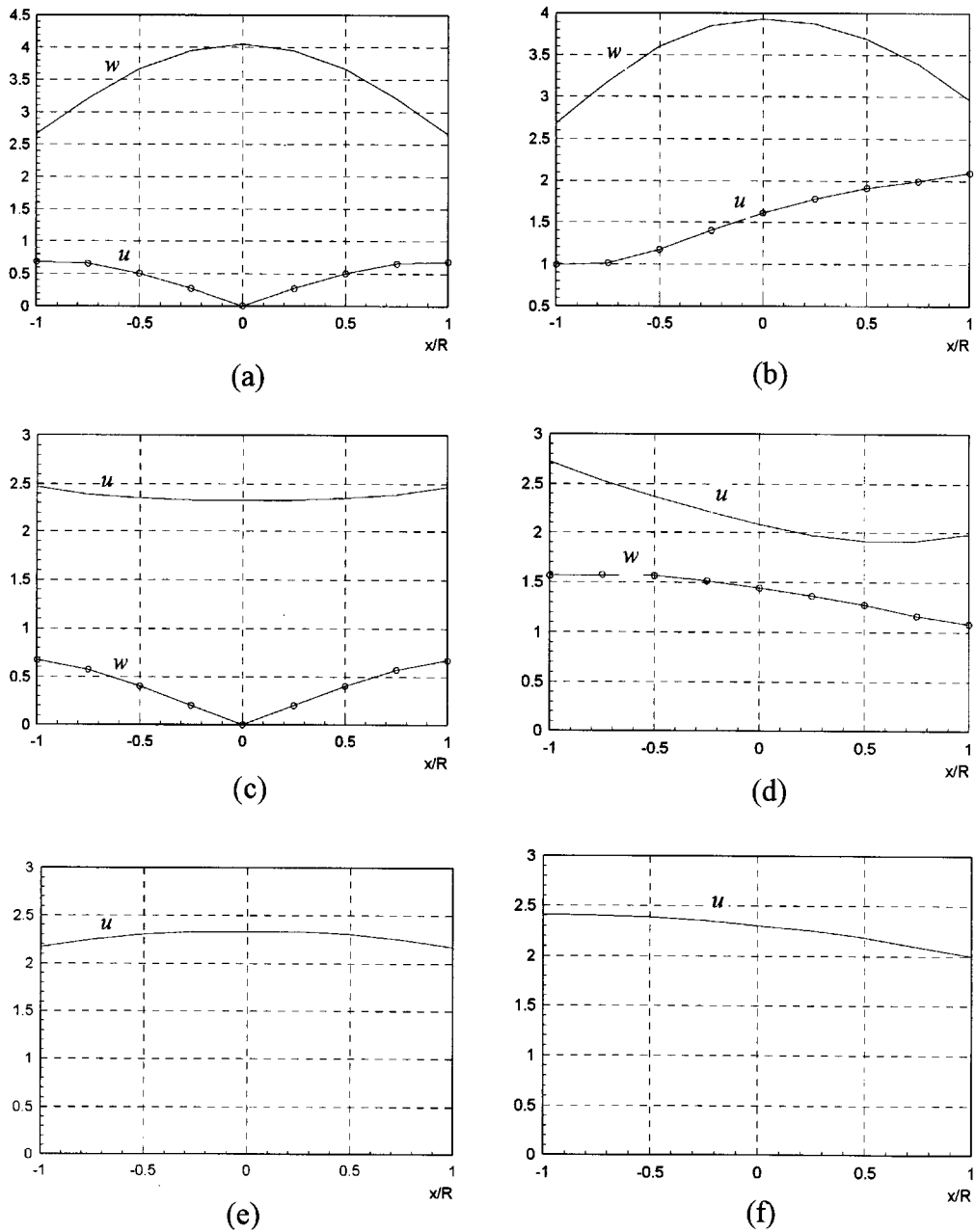


Figure 17. Surface amplitudes of a cubic deposit for incident waves at angle of incidence of 90 and 60°, respectively. (a) and (b) P-wave. Dimensionless frequency $\eta_p = 0.25$; (c) and (d) SV-wave. Dimensionless frequency $\eta_s = 0.25$; (e) and (f) SH-wave. Dimensionless frequency $\eta_s = 0.25$

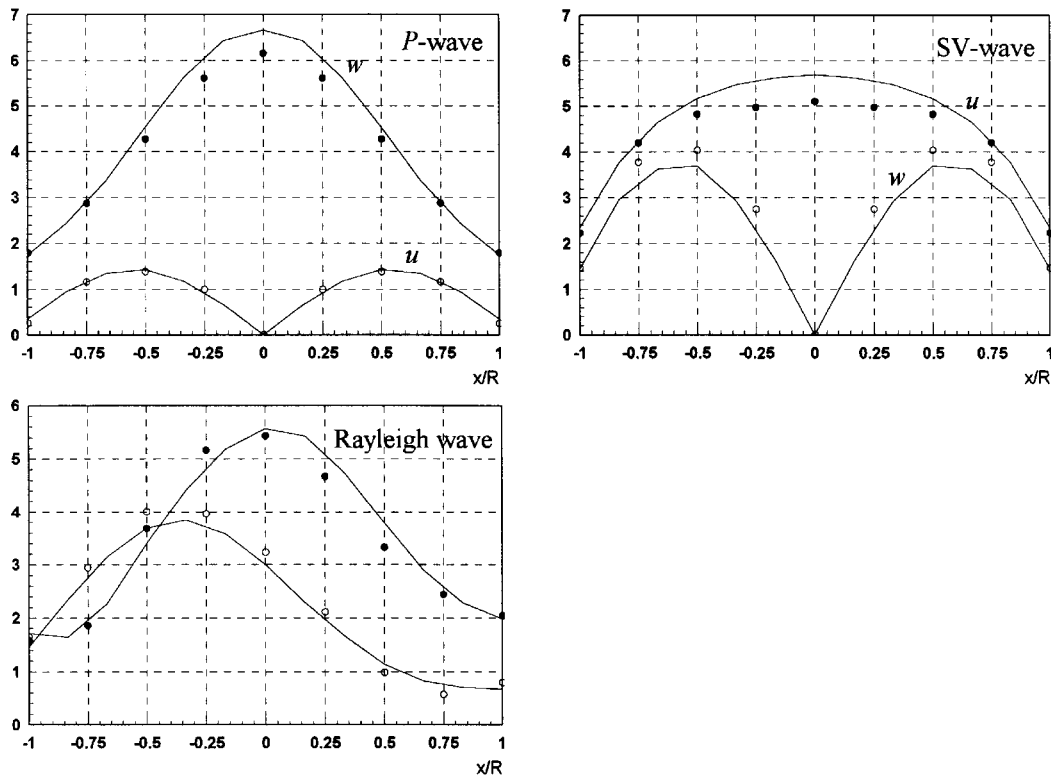


Figure 18. Surface amplitudes of a semicylindrical deposit for vertically incident P-, SV- and Rayleigh waves, respectively. Dimensionless frequency $\eta_s = 0.5$. Solid lines represent results obtained by the present method, while dots and circles represent results obtained by Dravinski¹⁷ for 2-D semicircular deposit

therefore the acceleration unit-impulse response matrix is sparse. The response matrix is approximated by five linear segments before dimensionless time $\bar{t}_k = 15 \cdot 10$ ($\bar{t}_k = \bar{t} \pi c_p / R$), and the dimensionless time step used for the calculation of the response matrix is 3.02. In order to compare the results with those in Reference 17, the dimensionless material properties of the half-space are taken to be: $G = 1$, $c_s = 1$, and $c_p = 2$, while the dimensionless material properties of the deposit are taken to be: $G = 1/6$, $c_s = 1/2$, and $c_p = 1$. Poisson's ratio for both materials is chosen to be $1/3$, and the radius of the deposit $R = 1$. Figure 18 presents the surface amplitudes of the deposit at stations along the x -axis for incident P-, SV- and Rayleigh-waves, for the dimensionless frequency $\eta_s = 0.5$.

6.7. Wave scattering by a hemispherical mountain

The scattering of a vertically incident SH wave by a hemispherical mountain is studied. The dimensionless parameters selected, are the same as for the hemispherical cavity. The finite-element model is generated by rotating Figure 19, 360° about the z -axis in 15° increments. The Point O is selected as the control point and the control motion is the harmonic motion with amplitude of 2.

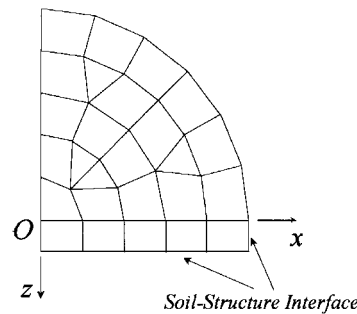


Figure 19. A section of the finite-element model for the hemispherical mountain

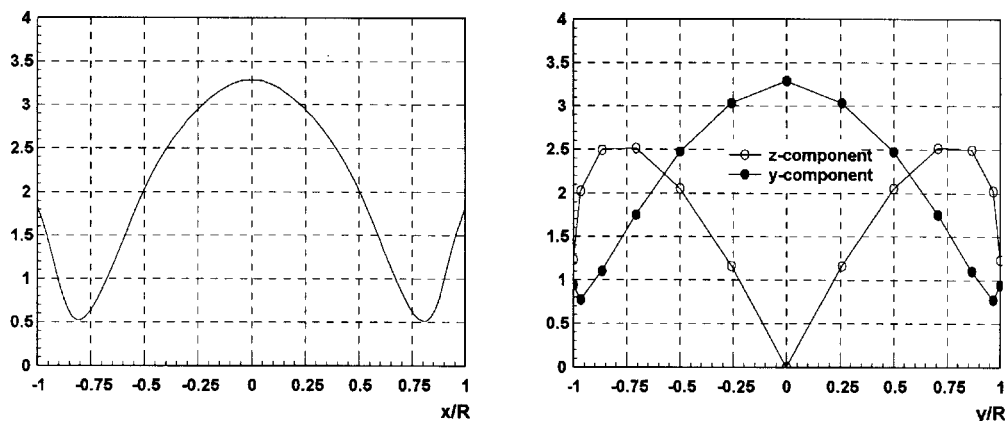
Figure 20. Surface displacement amplitudes at stations along the x - and y -axis, respectively

Figure 20 presents the surface displacement amplitudes of the mountain for the vertically incident SH wave at the stations along the x -axis, y -axis and the $x = y$ -axis, respectively.

7. CONCLUDING REMARKS

Three-dimensional dynamic soil–structure interaction analysis is a computationally intensive task, consequently it is desirable to develop efficient numerical procedures for engineering problems. The computational effort could be reduced to an acceptable level with only a little accuracy loss by using following strategies:

1. The unit-impulse response matrices are approximated by a few linear segments before time t_k , and approximated as a linear function of time after time t_k . This approximation results in a very efficient scheme for evaluation of the convolution integral which is a computationally intensive task in a soil–structure interaction analysis.
2. The structure–soil interface is divided into several substructures and the global unit-impulse response matrix, which is a sparse matrix, is obtained by assembling those for every

substructure. This approximation results in a significant reduction in computational effort for the calculation of the unit-impulse response matrix with little loss of accuracy.

3. The computational effort required for the calculation of the acceleration unit-impulse response matrix can be further reduced significantly by using a very large time step, say $t_k/5$, in the calculation of the acceleration unit-impulse response matrix. Usually, only four or five time steps are adequate.

The numerical procedure presented in this paper can be used to study the scattering and diffraction of incident seismic wave by any three-dimensional surface irregularities and other dynamic soil-structure interaction problems. Numerical studies show that the new scheme is applicable to earthquake engineering problems, for which the frequency range involved is usually below $\eta_p = 0.5$.

ACKNOWLEDGEMENTS

The authors would like to thank Dr John P. Wolf of the Swiss Federal Institute of Technology, Lausanne, for providing computer program SIMILAR, and thank Dr Chongmin Song of the Swiss Federal Institute of Technology, Lausanne, for his helpful discussion. The reviewer's critical and helpful comments are also highly appreciated.

REFERENCES

1. J. Lysmer and R. L. Kuhlemeyer, 'Finite dynamic model for infinite media', *J. Engng. Mech. Div. ASCE* **95**, 859–877 (1969).
2. W. D. Smith, 'A nonreflecting plane boundary for wave propagation problems', *J. Comput. Phys.* **15**, 492–503 (1974).
3. Z. P. Liao and H. L. Wong, 'A transmitting boundary for the numerical simulation of elastic wave propagation', *Soil Dyn. Earthquake Engng.* **3**, 174–183 (1984).
4. J. P. Wolf, *Dynamic Soil-Structure Interaction*, Prentice-Hall, Englewood Cliffs, NJ, 1985.
5. J. P. Wolf, *Soil-Structure-Interaction Analysis in Time Domain*, Prentice-Hall, Englewood Cliffs, NJ, 1988.
6. J. Chen, 'Analysis of local variations in free field seismic ground motion', *Ph.D. Dissertation*, University of California, Berkeley, 1980.
7. O. C. Zienkiewicz, D. W. Kelly and P. Betters, 'The coupling of the finite element methods and boundary solution procedures', *Int. J. Numer. Methods Engng.* **11**, 355–375 (1977).
8. O. Von Estorff and E. Kausel, 'Coupling of boundary and finite elements for soil-structure interaction problems', *Earthquake Engng. Struct. Dyn.* **18**, 1065–1075 (1989).
9. T. Touhei and T. Ohmachi, 'A FE-BE method for dynamic analysis of dam-foundation-reservoir system in the time domain', *Earthquake Engng. Struct. Dyn.* **22**, 195–209 (1993).
10. Ch. Song and J. P. Wolf, 'The scaled boundary finite-element method—alias consistent infinitesimal finite-element cell method-for elastodynamics', *Comput. Meth. Appl. Mech. Engng.* **147**, 329–355 (1997).
11. J. P. Wolf and Ch. Song, *Finite-Element Modelling of Unbounded Media*, Wiley, New York, 1996.
12. K. J. Bathe, *Finite Element Procedures*, Prentice-Hall, Englewood Cliffs, NJ, 1996.
13. V. W. Lee, 'Three-dimensional diffraction of plane P, SV & SH waves by a hemispherical alluvial valley', *Soil Dyn. Earthquake Engng.* **3**, 133–144 (1984).
14. F. J. Sánchez-Sesma, 'Diffraction of elastic waves by three-dimensional surface irregularities', *Bull. Seismol. Soc. Am.* **73**, 1621–1636 (1983).
15. H. Eshraghi and M. Dravinski, 'Scattering of plane harmonic SH, SV, P and Rayleigh waves by non-axisymmetric three-dimensional canyons: a wave function expansion approach', *Earthquake Engng. Struct. Dyn.* **18**, 983–998 (1989).
16. F. J. Sánchez-Sesma, L. E. Perez-Rocha and S. Chavez-Perez, 'Diffraction of elastic waves by three-dimensional surface irregularities, Part II', *Bull. Seismol. Soc. Am.* **79**, 101–112 (1989).
17. M. Dravinski, T. K. Mossessian, 'Scattering of harmonic P, SV, and Rayleigh waves by dipping layers of arbitrary shape', *Bull. Seismol. Soc. Am.* **77**, 212–235 (1987).
18. M. Dravinski, 'Scattering of SH waves by subsurface topography', *J. Engng. Mech. Div.* **108**, 1–16 (1982).

19. E. Reinoso, L. C. Wrobel and H. Power, 'Three-dimensional scattering of seismic waves from topographical structures', *Soil Dyn. Earthquake Engng.* **15**, 41–61 (1996).
20. H. L. Wong, 'Diffraction of P, SV, and Rayleigh waves by surface topographies', *Bull. Seismol. Soc. Am.* **72**, 1167–1184 (1982).
21. S. Kobayashi, 'Some problems of the boundary integral equation method in elastodynamics', in *Boundary Elements*, in C. A. Brebbia, T. Futagami, and M. Tanaka (eds), *Proc. 5th Int. Conf., Hiroshima, Japan*, Springer, New York, 1983, pp. 775–784.
22. A. H. Shah, K. C. Wong and S. K. Datta, 'Diffraction of plane SH waves in a half-space', *Earthquake Engng. Struct. Dyn.* **10**, 519–528 (1982).
23. T. K. Mossessian and M. Dravinski, 'Application of a hybrid method for scattering of P, SV, and Rayleigh waves by near-surface irregularities', *Bull. Seismol. Soc. Am.* **77**, 1784–1803 (1987).
24. E. Anderson, Z. Bai et al., *LAPACK User's Guide—Release 2.0*, Society for Industrial and Applied Mathematics, Philadelphia, PA, 1994.
25. A. Paronesso and J. P. Wolf, Global lumped-parameter model with physical representation for unbounded medium, *Earthquake Engng. Struct. Dyn.* **24**, 637–654, 1995.